J. Fluid Mech. (2022), *vol*. 953, A35, doi:10.1017/jfm.2022.978

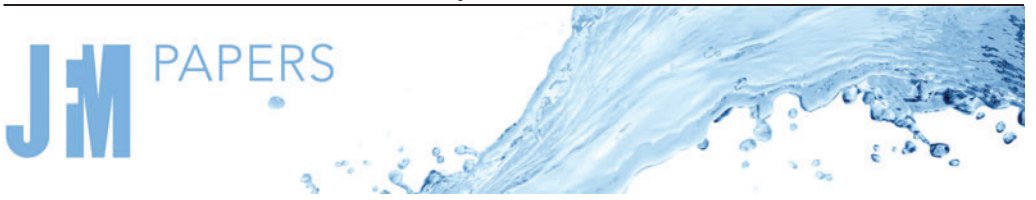

On the energy transport and heat transfer efficiency in radiatively heated particle-laden Rayleigh–Bénard convection

Wenwu Yang[1], **Zhen-Hua Wan**[2], **Quan Zhou**[1] **and Yuhong Dong**[1],†

[1]Shanghai Institute of Applied Mathematics and Mechanics, School of Mechanics and Engineering Science, and Shanghai Key Laboratory of Mechanics in Energy Engineering and Shanghai Frontier Science Center of Mechanoinformatics, Shanghai University, Shanghai 200072, PR China

[2]Department of Modern Mechanics, University of Science and Technology of China, Hefei 230027, PR China

(Received 29 June 2022; revised 17 October 2022; accepted 17 November 2022)

We investigate the energy transport and heat transfer efficiency in turbulent Rayleigh–Bénard (RB) convection laden with radiatively heated inertial particles. Direct numerical simulations combined with the Lagrangian point-particle mode were carried out in the range of density ratio $854.7 \leq \rho_p/\rho_0 \leq 8547$ and radiation intensity $1 \leq \phi/\phi_{solar} \leq 100$ for both two-dimensional (2-D) and three-dimensional (3-D) simulations. The Rayleigh number ranges from 2×10^6 to 10^8 for 2-D cases, and is 10^7 for 3-D cases for $Pr = 0.71$. It is found that particles with small density ratio that encounter strong radiation significantly alter the flow momentum transport and fluid heat transfer, so the fluid temperature of bulk is remarkably heated. We then derived the theoretical relation of the Nusselt number for interphase heat transfer in the heated particle-laden RB convection, which reveals that the heat transfer difference between the top and bottom plates stems from the interphase heat transfer. We further found that both the interphase heat transfer and the interphase thermal energy transport exhibit universal properties. They are both increased linearly with the reciprocal of the normalized density ratio. Additionally, both the interphase heat transfer and the interphase thermal energy transport increase linearly with the increase of radiation intensity. The growth rates exhibit specific scaling relations versus Rayleigh number and density ratio. Two different regimes distinguished by the critical density ratio, i.e. the exothermic particle regime and the endothermic particle regime, are observed. We further derived the power-law relation of the critical density ratios versus Rayleigh number and radiation intensity, i.e. $\rho_p/\rho_c \sim (\phi/\phi_{solar})^{1/2}\, Ra^{1/3}$, which is in remarkable agreement with the 3-D simulations.

Key words: particle/fluid flows, turbulent convection

† Email address for correspondence: dongyh@shu.edu.cn

1. Introduction

The particle-laden turbulent flow is a common scene in nature (Grabowski & Wang 2013) and engineering applications (Sahu, Hardalupas & Tayler 2014; Pouransari & Mani 2017). In this multi-phase flow system, the particle–turbulence interaction can significantly modulate the turbulence, and impact the kinetic and thermal behaviour of particles. This further results in various important dynamics (Elghobashi 1994; Balachandar & Eaton 2010) that are crucial in natural and industrial processes.

Particles of sufficient inertia in turbulence can concentrate in clusters away from vorticity core under the centrifugal effect and sweep-stick mechanism (Squires & Eaton 1991; Wang & Maxey 1993); they can also tend to cluster in the region close to the wall due to the turbophoresis in the wall-bounded flow (Reeks 1983; Bragg, Richter & Wang 2021). Thus the particles significantly alter the flow structures and the heat transfer of the flow. For instance, it is found that particles transfer their momentum to the small-scale flow, which increases the local velocity gradients (Ahmed & Elghobashi 2000) and further increases the viscous dissipation (Druzhinin & Elghobashi 1999). Moreover, Ferrante & Elghobashi (2003) found that the preferential concentration of settling particles significantly stretches the vortical structures in the gravitational direction, thus the turbulent energy redistributes from the horizontal to the vertical direction. Wang & Richter (2020) further investigated the multiscale interaction of inertial particles with turbulent flow structures in the turbulent channel flow. They highlight that the interaction between inertial particles and large-scale motions is crucial for the interphase energy transport. When the thermal buoyancy is negligible, the temperature is treated as a passive scalar. The modulation of fluid heat transfer and temperature field by particles are well investigated in the turbulent homogeneous shear flow and turbulent channel flow (Shotorban, Mashayek & Pandya 2003; Liu *et al.* 2018). Moreover, the multiscale thermal properties of particles and their contribution to fluid temperature are characterized (Carbone, Bragg & Iovieno 2019). In many conditions, the thermal buoyancy is very important and even is the driving force of the flow system. The single-phase buoyancy-driven flow, which is abstracted as the paradigmatic model Rayleigh–Bénard (RB) convection, has been investigated extensively (Ahlers, Grossmann & Lohse 2009; Lohse & Xia 2010; Wang, Zhou & Sun 2020). However, the study of particle-laden RB convection is a new field that has not been investigated widely. Oresta & Prosperetti (2013) found that the alteration of heat transfer is dominated by the thermal coupling for small particles, and the mechanical coupling plays an increasingly important role as the increasing of particle diameter in the cylindrical cell. Park, O'Keefe & Richter (2018) investigated the RB convection laden with non-isothermal particles in a three-dimensional rectangular cell, where particles are limited in the artificially tiny gravity. They found that the effect of preferential concentration results in the significant enhancement of the Nusselt number (Nu). Our recent work investigates the dynamic coupling between carrier fluid and particles in RB convection laden with particles (Yang *et al.* 2022*b*). We found that particles with medium Stokes number significantly enhance the Nusselt number due to strong coupling of the two phases, where the particle-induced kinetic energy is dominated.

As one of the strategies to utilize renewable energy efficiently, concentrating solar power (CSP) systems use low-cost materials to capture, store and transfer solar energy in the form of radiant heat through particulate two-phase flow, which can substantially reduce power generation costs and improve green energy supply. The particle solar receiver plays a key role in CSP, which can be regarded as a radiatively heated particle-laden two-phase flow (Tan & Chen 2010; Ho 2016). At present, some scholars have carried out some research for engineering applications. Chen *et al.* (2007) investigated numerically

the gas-particle flow in a solid-particle solar receiver. They found that particles with small size are easy to heat up, and higher temperatures can be achieved. Kim *et al.* (2009) studied the kinetic behaviour of heated particles in the solar particle receiver. They observed that the local concentration of particles results in the higher energy collection efficiency as it is more optically dense. Chinnici *et al.* (2015) investigated the particle residence time in the solar vortex reactor with different geometry. They found that the turbulent vortex structures strongly impact the resident time of particles. Researchers also abstracted the particle-based solar receivers as simpler multi-phase flow system to study the intrinsically physical mechanism. For instance, Pouransari & Mani (2017, 2018) found that the preferential concentration of heated particles reduces the heat transfer between particles and gas in a square channel. Rahmani *et al.* (2018) considered the particle polydispersity in a square channel. They found that the polydisperse heated particles perform better in transferring heat to the gas than the monodisperse particles. Frankel *et al.* (2016) analysed the influence of settling of heated particles on the turbulent structures in homogeneous turbulence. They found that the heated particles shed plumes of buoyant gas, which further modifies the turbulent structures. In this way, the turbulent kinetic energy varies non-monotonically as the increasing of radiation intensity due to the competing effects between the downward gravity and the upward buoyancy. Banko *et al.* (2020) investigated experimentally the temperature statistics in the heated particle-laden turbulent square duct flow. The temperature statistics exhibit qualitatively differently at the duct centreline and the near wall under the effect of preferential concentration of particles and the streamwise elongated streaks in the centre and the near-wall regions, respectively. Zamansky *et al.* (2014, 2016) investigated the turbulent thermal convection driven by heated inertial particles. They found that the fluid temperature properties and dissipation characteristics of energy are the result of the different forcing mechanisms that depend on the distribution of the particles. We note that works exploring the complete physics of particle–turbulence–radiation interaction are scarce, and the mechanisms and efficiency of energy transport in radiatively heated particle-laden flows are not well investigated. For example, little information exists that can address how the density ratio impacts exothermic and endothermic laws between phases. In addition, regarding the application of using solar radiant energy, the captured thermal energy tends to be high radiation intensity and causes considerable temperature differences in which the non-Oberbeck–Boussinesq effects should be considered, but this aspect is missing in previous studies. This has stimulated our enthusiasm to study related issues.

When fluid flow laden with solid particles is subject to radiative heating, it is often accompanied by the thermal buoyancy driving flow. There are temperature differences as well as strong thermal convection in the particle solar receiver; the radiatively heated particle-laden RB flow therefore can be regarded as one of the simplified models of particle solar receiver. To our knowledge, there is a lack of theoretical analysis on the interphase heat exchange of RB convection laden with heated particles, as well as an understanding of the relationship among particle motion, distribution, thermal variation of the flow field, and radiation intensity. Here, we focus on the energy transport characteristics and the heat transfer efficiency. We study numerically and theoretically the plate heat transfer and the interphase energy transport in the RB convection laden with heated particles, and investigate the correlation between particle–fluid density ratio versus Rayleigh number and radiation intensity.

The remainder of this paper is organized as follows. In § 2, we describe briefly the mathematical model and numerical procedure. Results and discussion are presented in § 3, which is divided into five parts. We describe the flow organization in § 3.1, and discuss the

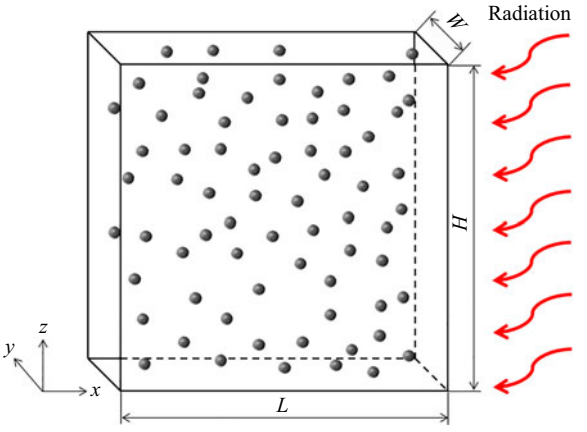

Figure 1. Configuration of turbulent RB convection laden with heated particles.

flow heat transfer and Reynolds number in § 3.2. In § 3.3, we derive the theoretical relation of the Nusselt number for the interphase heat transfer in a particle-laden RB convection system, and further analyse the specific relation between the interphase heat transfer and the normalized density ratio. Section 3.4 analyses the energy transport characteristics and discusses the kinetic energy and thermal energy. Section 3.5 discusses the scaling law of the critical density ratio versus the radiation intensity and the Rayleigh number. Finally, we give a conclusion for this work in § 4.

2. Mathematical model and numerical procedure

The configuration of the RB convection laden with heated particles is shown in figure 1, with cell width W, height H and depth D. We consider air as the working fluid; the temperature variation of fluid may be large under the effect of the heated particles, thus the fluid flow is governed by the low-Mach-number Navier–Stokes equations (Paolucci 1982). Additionally, the air is an optically transparent gas, thus we ignore the effect of thermal radiation on gas temperature. In addition, this work assumes that no portion of the radiation is absorbed or reflected by the cavity walls. That implies that all radiated heat is captured equally by the particles. The volume occupied by the particles is very small; we write the momentum equations and the energy equation, in dimensionless form, as

$$\frac{\partial \rho}{\partial t} + \frac{\partial \rho u_j}{\partial x_j} = 0, \tag{2.1}$$

$$\frac{\partial \rho u_i}{\partial t} + \frac{\partial \rho u_i u_j}{\partial x_j} = -\frac{\partial p}{\partial x_j} + \frac{1}{(Ra/Pr)^{1/2}} \frac{\partial \tau_{i,j}}{\partial x_j} + \frac{1}{2\varepsilon}(\rho - 1)\delta_{3i} + F_i, \tag{2.2}$$

$$\rho c_p \left(\frac{\partial T}{\partial t} + u_j \frac{\partial T}{\partial x_j} \right) = \frac{1}{(Ra\,Pr)^{1/2}} \frac{\partial}{\partial x_j} k \frac{\partial T}{\partial x_j} + \Gamma \frac{\mathrm{d}p_{th}}{\mathrm{d}t} + Q, \tag{2.3}$$

$$p_{th} = \rho T, \tag{2.4}$$

where ρ, u, T, p and p_{th} are, respectively, the fluid density, velocity, temperature, hydrodynamic pressure and thermostatic pressure; $\tau_{i,j} = \mu(\partial u_i/\partial x_j + \partial u_j/\partial x_i) - (2/3)\delta_{ij}\mu(\partial u_k/\partial x_k)$ is the viscosity stress tensor, where μ is the dynamical viscosity,

$\lambda = -2\mu/3$ is the volume viscosity, and δ_{ij} is the Kronecker delta; c_p is the isobaric specific heat and is fixed at unity; $\Gamma = (\gamma - 1)/\gamma$ represents the resilience of the fluid, with the ratio of specific heats $\gamma = 1.4$. The dimensionless thermal conductivity k and dynamic viscosity μ for air are governed by Sutherland's law

$$k = T^{1.5}(1 + S_k)/(T + S_k), \quad \mu = T^{1.5}(1 + S_\mu)/(T + S_\mu), \tag{2.5a,b}$$

where $S_k = 0.648$ and $S_\mu = 0.368$ for the reference temperature $T_0 = 300\,\mathrm{K}$ (Suslov & Paolucci 1999; Suslov 2010). Sutherland's law is developed based on the kinetic theory of ideal gases and an idealized intermolecular force potential (Sutherland 1893), thus fairly accurate results can be obtained with an error less than a few per cent over a wide range of temperatures. The terms F_i and Q, respectively, represent the momentum and thermal feedback of the dispersed phase, which will be described later. The non-dimensional equations (2.1)–(2.4) are obtained by the cell height H, the arithmetic average temperature T_0, the averaged density ρ_0, the characteristic velocity $u^* = (2\varepsilon g H)^{1/2}$, and the reference thermodynamic pressure $\rho_0 R T_0$, where g is the acceleration due to gravity, and R is the gas constant. The fluid properties at the reference temperature and the thermodynamic pressure are also the reference quantities, including $c_{p,0}$, μ_0 and k_0. The dimensionless temperature differential ε, the Rayleigh number and the Prandtl number are defined as

$$\varepsilon = \frac{\Delta T}{2T_0}, \quad Ra = \frac{2\varepsilon c_{p,0}\rho_0^2 g H^3}{\mu_0 k_0}, \quad Pr = \frac{c_{p,0}\mu_0}{k_0}. \tag{2.6a–c}$$

In this work, the particles in air are highly dilute and optically thin, thus we can neglect particle–particle interaction (Elghobashi 1994, 2019) and assume that every particle receives the same amount of radiation (Frankel, Iaccarino & Mani 2017). In addition, the density of particles is much higher than that of the fluid, and particle diameters are small compared with the Kolmogorov scale of turbulence. All the constant properties of the simulations are shown in table 1. Under the above assumptions, movement of particles is conducted by Stokes drag and gravity (Elghobashi & Truesdell 1992; Guha 2008; Balachandar & Eaton 2010). Therefore, we write the particle equations, in dimensionless form, as

$$\frac{\mathrm{d}x_{p,i}}{\mathrm{d}t} = u_{p,i}, \tag{2.7}$$

$$\frac{\mathrm{d}u_{p,i}}{\mathrm{d}t} = -\frac{1}{Fr_p^2}\,\delta_{3i} - \frac{C_D}{St_f}\,(u_{p,i} - u_i), \tag{2.8}$$

$$\frac{\mathrm{d}T_p}{\mathrm{d}t} = \frac{Nu_p}{2}\,\frac{T_f - T_p}{St_T} + q, \tag{2.9}$$

where x_p, u_p and T_p are the particle dimensionless position, velocity and temperature, respectively; T_f is the fluid temperature at the particle location; $Fr_p = (2\varepsilon)^{1/2}$ represents the ratio of inertia force of fluid to gravity of a particle; $C_D = 1 + 0.15\,Re_p^{0.678}$ represents the drag correction coefficient that applies when the particle Reynolds number $Re_p = (d_p/H)(\rho/\mu)\,|\boldsymbol{u} - \boldsymbol{u}_p|\,(Ra/Pr)^{1/2}$ exceeds unity, where d_p is the particle diameter, and the notation $|\boldsymbol{u} - \boldsymbol{u}_p|$ refers to the magnitude of the vector difference between the fluid and particle velocities. The particle Nusselt number Nu_p is given by a well-known empirical correlation as $Nu_p = 2 + 0.6\,Re_p^{1/2}\,Pr^{1/3}$ (Ranz & Marshall 1952). The particle Stokes number and the thermal Stokes number based on the

Parameters	Value
Prandtl number, Pr	0.71
Aspect ratio, H/D	1
Reference temperature, T_0	300 K
Temperature difference, ΔT	60 K
Reference density, ρ_0	$1.17\,\mathrm{kg\,m^{-3}}$
Dynamical viscosity, μ_0	$1.84 \times 10^{-5}\,\mathrm{kg\,(m\,s)^{-1}}$
Thermal conductivity, k_0	$2.60 \times 10^{-2}\,\mathrm{W\,(m\,K)^{-1}}$
Fluid specific heat, $c_{p,0}$	$1005\,\mathrm{J\,(kg\,K)^{-1}}$
Particle specific heat, $c_{p,p}$	$700\,\mathrm{J\,(kg\,K)^{-1}}$
Particle diameter, d_p	40 μm
Mass loading, Φ_m	0.01

Table 1. Summary of the fluid and particle properties used in the simulation. Here, the heights of the convection cell are 0.07, 0.12 and 0.26 m for $Ra = 2 \times 10^6$, 10^7 and 10^8, respectively.

integral time scale are given by $St_f = (1/18)(\rho_p/\rho_0)(d_p/H)^2(\mu_0/\mu)(Ra/Pr)^{1/2}$ and $St_T = (1/12)(c_{p,p}/c_{p,0})(\rho_p/\rho_0)(d_p/H)^2(k_0/k)(Ra\,Pr)^{1/2}$, respectively, where ρ_p denotes the particle density. In this study, the non-Oberbeck–Boussinesq effect is considered, thus the thermal conductivity k and dynamic viscosity μ are not constants. That is, both Stokes numbers vary with the location of particles in the cell. They represent respectively the inertia and the thermal inertia of a particle in turbulence. Here, $q = \phi_p/\phi_p^*$ is the heat absorption by a particle with the radiation intensity ϕ, where $\phi_p = (\pi/4)d_p^2\phi$ and $\phi_p^* = c_{p,p}m_pT_0/(H/(2\varepsilon g))^{1/2}$, and m_p is the mass of a particle.

According to previous studies, in the case of particle mass fraction in table 1, the interaction between particles and fluid is significant, thus particles change the turbulent structures (Elghobashi & Truesdell 1992). The size of particles is far less than the Kolmogorov scale of the flow field, so the point-particle model applies. In (2.2) and (2.3), F_i and Q respectively represent the total force and heat exerted on the fluid by the point-particle in each fluid cell (Oresta & Prosperetti 2013; Liu *et al.* 2018). Thus F_i and Q are expressed as

$$F_i = -\frac{\pi}{6}\frac{\rho_p}{\rho_0}\frac{d_p^3}{V}\sum_{j=1}^{N}\left(\frac{\mathrm{d}u_{p,i}^j}{\mathrm{d}t} - \left(-\frac{1}{Fr_p^2}\,\delta_{3i}\right)\right), \tag{2.10}$$

$$Q = -\frac{\pi}{6}\frac{c_{p,p}}{c_{p,0}}\frac{\rho_p}{\rho_0}\frac{d_p^3}{V}\sum_{j=1}^{N}\left(\frac{\mathrm{d}T_p^j}{\mathrm{d}t} - q\right), \tag{2.11}$$

where V is the fluid volume of the cell, and N is the number of particles in the cell.

The RB convection models that we consider here are both two-dimensional (2-D) and three-dimensional (3-D). For the 2-D cases, it can be an approximate cross-section of the two-phase flow in a square pipe with $H/L = 1$. Here, we consider the fluid layer thickness in the y-direction W to be very thin, with $W = H/(N_p)^{1/2}$, and N_p is the total number of particles. In this way, on average, a specific particle will occupy a 3-D box with sides equal to $H/(N_p)^{1/2}$. The coupling between fluid and particle features is 3-D to some extent, while the flow characteristics tend to be generally 2-D. The reasonableness of this approximation includes mainly the following. (i) Many well-cited theories for

turbulent RB systems are essentially 2-D, e.g. the popular Grossmann–Lohse theory (Grossmann & Lohse 2000) and the Whitehead–Doering theory for the ultimate regime (Whitehead & Doering 2011). (ii) The 2-D turbulence has been a possible application to intermediate-scale meteorological flow (Kraichnan 1967), and it can be used to better understand the physical mechanisms of 3-D convection (van der Poel, Stevens & Lohse 2013). (iii) Many of the important physical processes found in 3-D flows laden with inertial particles are also present in the 2-D model (Patočka, Calzavarini & Tosi 2020; Xu *et al.* 2020). For the 3-D cases, the geometry of the flow system is a cavity with $H/L = 1$ and $H/W = 1$. For both the 2-D and 3-D cases, the bottom and top walls are respectively fixed at constant temperatures $1 + \varepsilon$ and $1 - \varepsilon$, while the lateral walls are assumed to be thermally adiabatic; in addition, no-penetration and no-slip velocity boundary conditions are applied to all solid walls. Here, we study both the 2-D and 3-D cases to compare the similarities and the differences of heat transfer as well as the energy transport mechanism in different geometries.

The governing equations (2.1)–(2.3) are discretized using the second-order central difference method. The fractional-step method is used to solve the equations (Verzicco & Orlandi 1996). A multi-grid strategy (Briggs, Henson & McCormick 2000) is adopted to solve the pressure Poisson equation. For time advancement, the wall-normal viscous terms are treated semi-implicitly with the Crank–Nicolson scheme, while all other terms are discretized by the third-order Runge–Kutta scheme. The numerical details and validations of the code have been elaborated in previous works (Xia *et al.* 2016; Liu *et al.* 2018; Wang *et al.* 2019). After the flow field is fully developed, particles are injected into the flow field at a random position, with their velocities and temperatures set to those of the local fluid, then we continue the simulation of the particle-laden flow. In the computation, Lagrangian particle tracking is employed to obtain the position and the velocity of the particles. Equations of particles' evolution are advanced in time by a second-order Adams–Bashforth method (Dong & Chen 2011). For particles, an elastic reflection is enforced at the upper wall and the lateral walls. When a particle reaches the bottom of the cell, it is removed from the calculation and a new particle is re-injected at a random position on the top plate with velocity zero and temperature $1 - \varepsilon$, which is the same as the top temperature. This assumption means that the volume fraction of discrete phases in the system remains unchanged, and each particle injected is always at the same temperature as the surrounding fluid. The present particle re-entry model was supported by previous numerical studies (Oresta & Prosperetti 2013). In fact, newly injected particles here do not represent the subsequent behaviour of removing particles. The thermal modulation at small scales can be due only to the local non-uniformity of the thermal coupling between interphases. The momentum and energy of the carrier phase and discrete phase can be in equilibrium. Generally speaking, this approximation is reasonable when the residence time of the particles in the flow is short, in view of the comparatively smaller volumetric heat capacity of the fluid. To reveal systematically the properties of the heat transfer and energy transport in the heated particle-laden RB convection, we carried out both 2-D and 3-D direct numerical simulations (DNS) cases as shown in table 2, where radiation intensity is $1 \leq \phi/\phi_{solar} \leq 100$, spanning the density ratio range $854.7 \leq \rho_p/\rho_0 \leq 8547$. All the simulations are performed at fixed Prandtl number $Pr = 0.71$, Froude number $Fr_p = 0.447$, mass loading $\Phi_m = 0.01$, temperature differential $\varepsilon = 0.1$, and particle diameter $d_p = 40\,\mu\text{m}$. We adopt the non-uniform grid with more grid points clustered near walls to achieve a full resolution of the boundary layer and the smallest scale of the flow. For 2-D DNS cases, the grid numbers are set to be $N_x \times N_z = 256 \times 256$, 384×384 and 768×768 for $Ra = 2 \times 10^6$, 10^7

	2-D	3-D
Ra	$2 \times 10^6, 10^7, 10^8$	10^7
ϕ	$\phi_{solar} \leq \phi \leq 100 \times \phi_{solar}$	
ρ_p/ρ_0	$854.7 \leq \rho_p/\rho_0 \leq 8547$	
Φ_V	$1.17 \times 10^{-5} \leq \Phi_V \leq 1.17 \times 10^{-4}$	

Table 2. Simulation parameters. For all cases, the Prandtl number is $Pr = 0.71$, the Froude number is $Fr_p = 0.447$, the mass loading is $\Phi_m = 0.01$, the temperature differential is $\varepsilon = 0.1$, and the particle diameter is $d_p = 40\,\mu\text{m}$.

and 10^8, respectively. For 3-D cases, $Ra = 10^7$ and $N_x \times N_y \times N_z = 192 \times 192 \times 192$ were used.

3. Results

3.1. *Flow organization*

The instantaneous temperature field and flow structures in the 2-D convection cell at $Ra = 10^7$ and $\phi = 50 \times \phi_{solar}$ for the single-phase case and the particle-laden cases with three density ratios, i.e. $\rho_p/\rho_0 = 2564.1$, 4273.5 and 8547.0, are shown in figures 2(*a–d*). In the 2-D simulations, a large-scale circulation accompanied by small secondary rolls is observed in the single-phase case in figure 2(*a*); the thermal plumes self-organize into a large-scale coherent structure, and move along side walls (Xu *et al.* 2021). For the small-density-ratio case $\rho_p/\rho_0 = 2564.1$, there are more secondary rolls as the flow is speeded up by the particle cluster, as shown in figure 2(*b*). This is in line with the observation of our previous work in the RB convection laden with isothermal particles (Yang *et al.* 2022*b*). Moreover, the temperature of bulk increases significantly due to the heated particles transferring their heat to the fluid. The flow structures and the temperature field vary a little at the medium-density-ratio case $\rho_p/\rho_0 = 4273.5$. For the large-density-ratio case $\rho_p/\rho_0 = 8547.0$, the flow structures change a small amount. The temperature of the bulk surprisingly drops a little, which implies that the heated particles absorb heat from the fluid. In the 3-D simulations, vigorous sheet-like plumes are ejected from the bottom and top plates, as shown in figure 2(*e*). For the particle-laden case at the small density ratio $\rho_p/\rho_0 = 2564.1$, the hot plumes stretch into the bulk, which indicates that the bulk is heated significantly.

Additionally, the distribution of particles is also given in figures 2(*b–d*) for 2-D cases, and figure 2(*e*) for 3-D simulation. For small density ratio $\rho_p/\rho_0 = 2564.1$, particles cluster into bands along the edge of the large-scale circulation as the effect of preferential sweeping (Wang & Maxey 1993) for the 2-D case, as shown in figure 2(*b*). The clusters that act on the edge of the eddy can change the strength and shape of the eddy, as shown in figure 2(*b*). This is decided by the transport patterns of particles. Particles with a particular density ratio (or Stokes number) can cluster into bands that correlate to the edges of eddies, which is named as channel transport mode (Yang *et al.* 2022*a*). The preferential concentration of particles is also observed repeatedly for RB convection, mixing layer and jet flow (Lázaro & Lasheras 1992; Longmire & Eaton 1992). But in the 3-D case, the distribution of particles is uniform, as shown in figure 2(*e*), as the flow strength is rather weaker than in the 2-D case, and the preferential sweeping cannot significantly impact

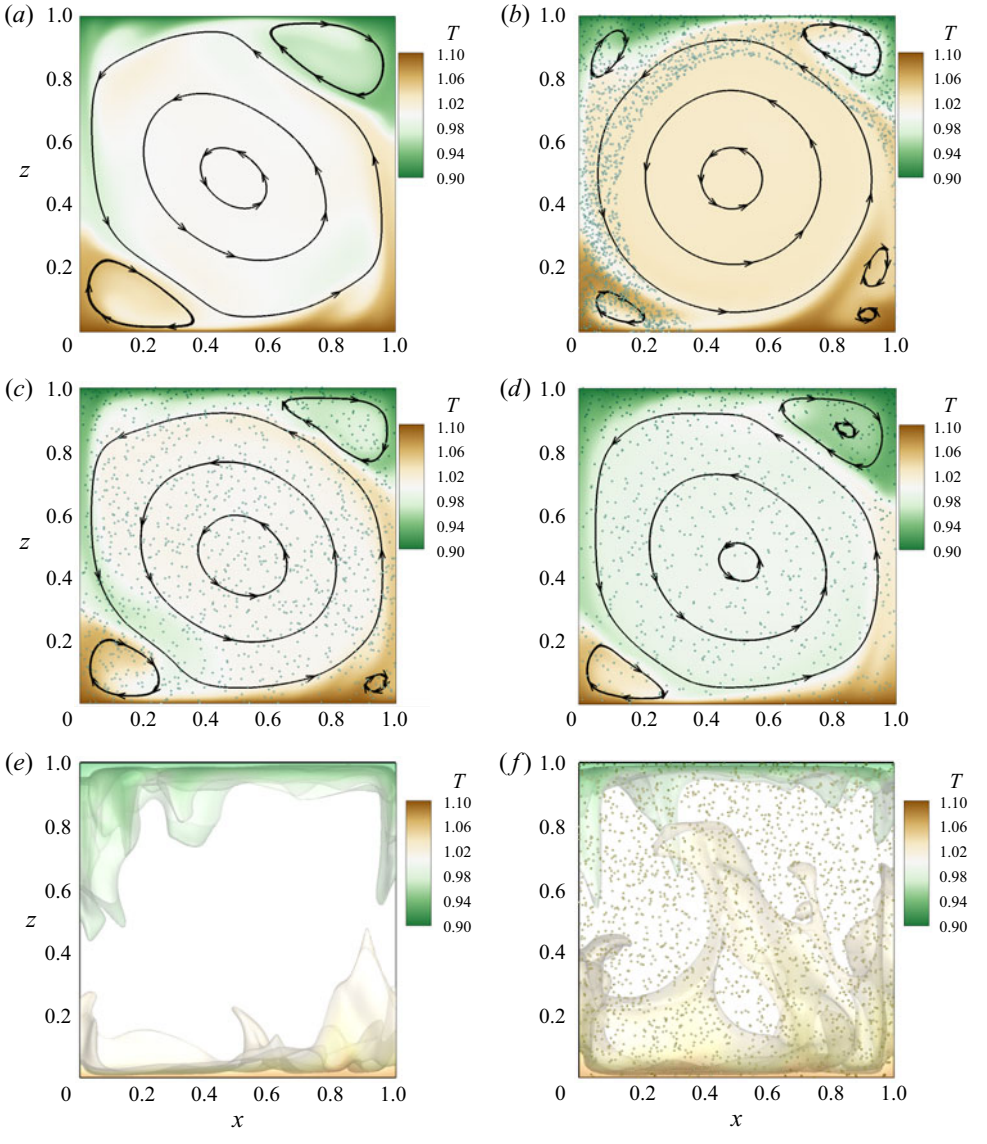

Figure 2. Typical snapshots of the 2-D instantaneous temperature field (colour) and streamlines (black lines with arrows) for $Ra = 10^7$ at $Pr = 0.71$, $\varepsilon = 0.1$ and $\phi = 50 \times \phi_{solar}$: (*a*) single-phase, (*b*) $\rho_p/\rho_0 = 2564.1$, (*c*) $\rho_p/\rho_0 = 4273.5$, and (*d*) $\rho_p/\rho_0 = 8547.0$. (*e*,*f*) Instantaneous temperature isosurfaces of 3-D cases with the opacity set to be 50 % and the distribution of particles for $Ra = 10^7$ at $Pr = 0.71$, $\varepsilon = 0.1$ and $\phi = 50 \times \phi_{solar}$: (*e*) single-phase, (*f*) $\rho_p/\rho_0 = 2564.1$. Here, 50 % and 1 % of the total number of particles are shown for the 2-D cases and 3-D case, respectively.

the distribution of particles. For the medium and large density ratios $\rho_p/\rho_0 = 4273.5$ and 8547.0, the particle motion is dominated by its gravity; consequently, the distribution of particles has no significant correlation with the structures of eddies, and particles distribute uniformly in the flow field, as shown in figures 2(*c*,*d*).

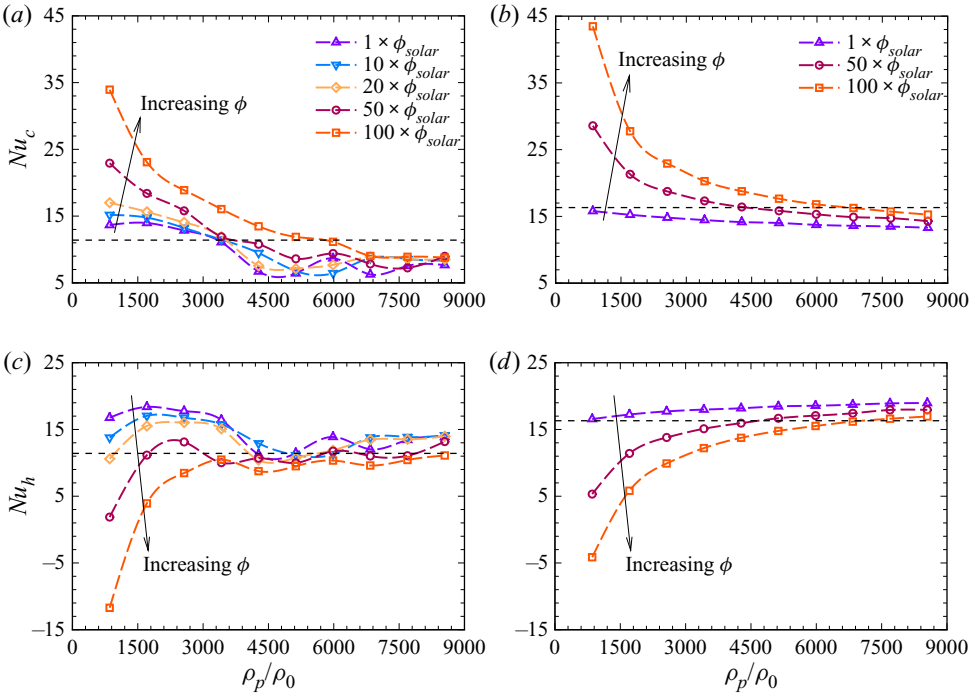

Figure 3. Cold-plate Nusselt number Nu_c as a function of density ratio ρ_p/ρ_0 for (*a*) 2-D cases and (*b*) 3-D cases. Hot-plate Nusselt number Nu_h as a function of density ratio ρ_p/ρ_0 for (*c*) 2-D cases and (*d*) 3-D cases. For all the cases, $Ra = 10^7$, $Pr = 0.71$ and $\varepsilon = 0.1$. The black dashed lines denote the volume-averaged Nusselt number for 2-D and 3-D single-phase cases.

3.2. *Flow heat transfer and Reynolds number*

The cold-plate Nusselt number and the hot-plate Nusselt number are shown in figure 3. For the cold-plate Nusselt number Nu_c as shown in figures 3(*a*,*b*), Nu_c is decreased almost monotonically as the increase of the density ratio ρ_p/ρ_0, and it also noted that Nu_c becomes larger for large radiation intensity. The trends between the 2-D cases and the 3-D cases are basically the same. The particles with a small density ratio and large radiation intensity can substantially increase the cold-plate heat transfer of the convection cell; this implies that in this situation, the temperature of particles is significantly larger than that of the cold plate, thus it becomes important that the heat transfers between the hot particles and the top plate. For the hot-plate Nusselt number Nu_h as shown in figures 3(*c*,*d*), there is little difference between the 2-D cases and 3-D cases. For the 2-D cases, Nu_h climbs to a peak then goes down near the heat transfer of the single-phase case with increasing density ratio, when the radiation intensity is lower than $50 \times \phi_{solar}$. At larger radiation intensity, for example, $\phi = 100 \times \phi_{solar}$ as shown in figure 3(*c*), Nu_h increases monotonically to the heat transfer of the single-phase case with increasing density ratio. Note that slight 'bump-like' variations can be observed in the Nusselt numbers at high density ratios in figures 3(*a*,*c*). This is related to thermal and mechanical fluid–particle coupling. The acceleration that the particles impart to the colder, descending fluid stream is re-balanced by the retardation that they cause on the warmer fluid. Meanwhile, the larger drag that they impose on the flow in the thermal boundary layers is responsible for the decline of Nu_c in the bump-like variation at high density ratio. For the 3-D cases, Nu_h becomes monotonically larger for

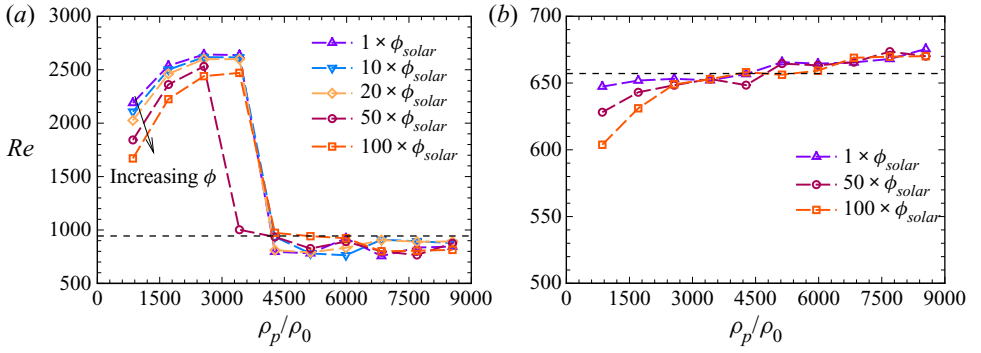

Figure 4. *Re* as functions of ρ_p/ρ_0 for different values of radiation intensity for (*a*) 2-D cases and (*b*) 3-D cases, for $Ra = 10^7$ at $Pr = 0.71$ and $\varepsilon = 0.1$.

the large density ratio, and reaches a value that is slightly larger than the heat transfer of the single-phase case. Moreover, for both the 2-D cases and 3-D cases, it is noted that Nu_h can become negative, with a very large absolute value at small density ratio and large radiation intensity, which means that a large heat flux goes down. This implies that the temperature of the heated particle at a small density ratio and large radiation intensity is significantly larger than the hot-plate temperature; consequently, heat is transported from particles with a higher position than the bottom wall to the hot plate. What is more, as the density ratio becomes very large, the dependence of Nu_c (or Nu_h) on the radiation intensity becomes inconspicuous.

The heated particles also change significantly the turbulent momentum transport. The Reynolds number (*Re*) of the thermal convection system can imply the activity of the turbulent momentum, and is calculated as $Re = U_{rms}(Ra/Pr)^{1/2}$, where $U_{rms} = \langle \boldsymbol{u} \cdot \boldsymbol{u} \rangle^{1/2}$, in which $\langle \cdot \rangle$ denotes an ensemble (or space–time) average. We show *Re* for different density ratios and radiation intensities in figures 4(*a*,*b*). For the 2-D cases, *Re* is increased significantly, by up to 280 % for small density ratio as the particle clusters acting on the edges of the eddy, called a circling transport pattern, as shown in figure 2(*b*), vastly accelerate the motion of the fluid and then enhance the turbulent momentum transport of the cell. In addition, a significant decline of *Re* is observed for large-density-ratio cases, where particles settle uniformly due to large inertia, called a downpour transport pattern, as shown in figures 2(*c*,*d*). Particles cannot transfer their momentum effectively to fluid, instead increasing the dissipation of fluid kinetic energy, and causing a substantial change in the Reynolds number. Our recent work (Yang *et al.* 2022*a*) found that the flow structure and heat transfer processes can change significantly with different particle motion patterns. This also implies that the buoyancy contribution from heated particles is less for large-density-ratio particle-laden cases. For the 3-D cases, the physical model and the boundary conditions (especially the constraints on the front and back walls) are different from the 2-D cases. Particle clusters and the aforementioned particle transport patterns are not observed within the current parameters; the particles tend to be distributed uniformly in the flow field at all times – see figure 2(*f*). Thus the Reynolds number shows a continuous variation following the density ratio, and it is less than the single-phase Reynolds number for small density ratio (small inertia particles). This is in line with the observations in a cylindrical RB convection system by Oresta & Prosperetti (2013).

3.3. *Interphase heat transfer efficiency*

The interphase heat transfer is one of the key focuses in the RB convection laden with heated inertial particles. It is strongly related to how to exchange and store thermal energy in the particle solar receiver flow system. Here, based on the energy equation and the continuity equation of fluid, we derive the theoretical relation between the cold/hot plate heat transfer and the interphase heat transfer. The fluid continuity equation and the energy equation are given as equations (2.1) and (2.3). Here, for a closed system with no-slip and no-penetration boundary conditions, the time derivative of thermodynamic pressure is

$$\frac{\mathrm{d}p_{th}}{\mathrm{d}t} = \frac{1}{(Ra\,Pr)^{1/2}}\frac{1}{(1-\Gamma)V}\int_S k\frac{\partial T}{\partial x_j}n_j\,\mathrm{d}S. \tag{3.1}$$

We combine this with the time-averaged fluid continuity equation (2.3) to get

$$c_p\left(\frac{\partial(\rho T)}{\partial t}+\frac{\partial(\rho u_j T)}{\partial x_j}\right) = \frac{1}{(Ra\,Pr)^{1/2}}\frac{\partial}{\partial x_j}k\frac{\partial T}{\partial x_j}+\Gamma\frac{\mathrm{d}p_{th}}{\mathrm{d}t}+Q. \tag{3.2}$$

Applying stationarity (i.e. the first term on the left-hand side equals zero) and the z-plane average for (3.2), and combining the no-penetration boundary condition at all side walls, $\int_A(\partial(\rho uT)/\partial x+\partial(\rho vT)/\partial y)\,\mathrm{d}x\,\mathrm{d}y$ vanishes; $\int_A((\partial/\partial x)k(\partial T/\partial x)+(\partial/\partial y)k(\partial T/\partial y))\,\mathrm{d}x\,\mathrm{d}y=0$ as there is no heat flux at all side walls.

Thus

$$\left\langle c_p\frac{\partial(\rho wT)}{\partial z}\right\rangle_{A,t} = \frac{1}{(Ra\,Pr)^{1/2}}\left\langle\frac{\partial}{\partial z}k\frac{\partial T}{\partial z}\right\rangle_{A,t}+\left\langle\Gamma\frac{\mathrm{d}p_{th}}{\mathrm{d}t}\right\rangle_{A,t}+\langle Q\rangle_{A,t}, \tag{3.3}$$

where $\langle\cdot\rangle_{A,t}$ denotes the z-plane time average. We use the given definitions of Nu_c and Nu_h to write

$$Nu_c = \left\langle\left(-k_d\frac{\partial T_d}{\partial z_d}\right)\Big|_H \Big/ \left(k_0\frac{\Delta T}{H}\right)\right\rangle_{A,t} = -\frac{k}{2\varepsilon}\left\langle\frac{\partial T}{\partial z}\right\rangle_{A,t}\Big|_1, \tag{3.4}$$

$$Nu_h = \left\langle\left(-k_d\frac{\partial T_d}{\partial z_d}\right)\Big|_0 \Big/ \left(k_0\frac{\Delta T}{H}\right)\right\rangle_{A,t} = -\frac{k}{2\varepsilon}\left\langle\frac{\partial T}{\partial z}\right\rangle_{A,t}\Big|_0. \tag{3.5}$$

Then we perform the integration over $0\le z\le z_1$ and $z_1\le z\le 1$. We can obtain the non-dimensional heat flux of the hot plate and cold plate as

$$\begin{aligned} Nu_h = {} & \frac{(Ra\,Pr)^{1/2}}{2\varepsilon}\langle\rho wT\rangle_{A,t}\Big|_{z_1} - \left\langle\frac{k(z_1)}{2\varepsilon}\frac{\partial T}{\partial z}\right\rangle_{A,t}\Big|_{z_1} \\ & - \frac{(Ra\,Pr)^{1/2}}{2\varepsilon}\int_0^{z_1}\langle Q\rangle_{A,t}\,\mathrm{d}z - (\gamma-1)z_1\,(Nu_c-Nu_h), \end{aligned} \tag{3.6}$$

$$\begin{aligned} Nu_c = {} & \frac{(Ra\,Pr)^{1/2}}{2\varepsilon}\langle\rho wT\rangle_{A,t}\Big|_{z_1} - \left\langle\frac{k(z_1)}{2\varepsilon}\frac{\partial T}{\partial z}\right\rangle_{A,t}\Big|_{z_1} \\ & + \frac{(Ra\,Pr)^{1/2}}{2\varepsilon}\int_{z_1}^{1}\langle Q\rangle_{A,t}\,\mathrm{d}z + (\gamma-1)(1-z_1)\,(Nu_c-Nu_h). \end{aligned} \tag{3.7}$$

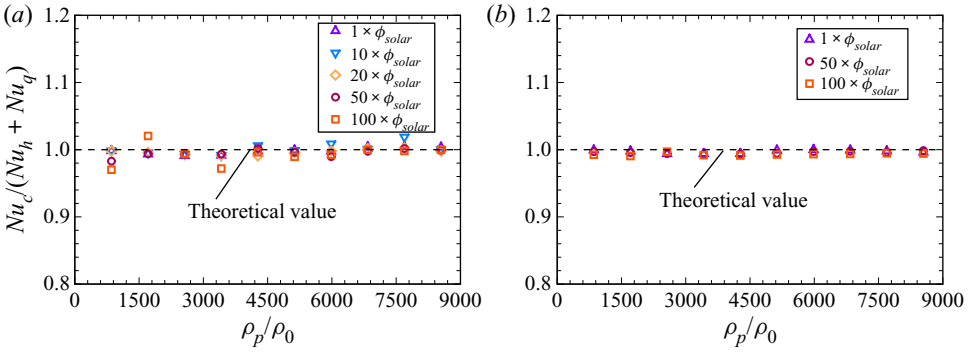

Figure 5. $Nu_c/(Nu_h + Nu_q)$ as functions of ρ_p/ρ_0 for different values of radiation intensity at $Ra = 10^7$ for (*a*) 2-D cases and (*b*) 3-D cases.

Equation (3.7) minus (3.6) gives

$$Nu_c - Nu_h = \frac{(Ra\,Pr)^{1/2}}{2\varepsilon\gamma}\int_0^1 \langle Q\rangle_{A,t}\,\mathrm{d}z$$
$$= -\frac{(Ra\,Pr)^{1/2}}{2\varepsilon\gamma}\,\frac{\pi}{6}\,\frac{c_{p,p}}{c_{p,0}}\,\frac{\rho_p}{\rho_0}\,\frac{d_p^3}{HLW}\left\langle\sum_{i=1}^{N}\left(\frac{\mathrm{d}T_{p,i}}{\mathrm{d}t} - q\right)\right\rangle_t = Nu_q. \tag{3.8}$$

Here, Nu_q denotes the difference between the Nusselt numbers of the cold and hot plates. Equation (3.8) shows that Nu_q is the result of the interphase heat transfer in the cell. We can also verify our numerical resolution utilizing (3.8). Figure 5 compares Nu_c and $Nu_h + Nu_q$ for various density ratios at different radiation intensities and at fixed $Ra = 10^7$. It is seen from the figure that $Nu_c/(Nu_h + Nu_q)$ is quite close to unity for different radiation intensities and density ratios, which indicates that the grid resolutions are fine enough to obtain accurate results that are very close to the theory results, and the small flow structures can be well captured. What is more, it also indicates that both the momentum feedback and the thermal feedback imposed by the heated particles are properly calculated.

We further plot the variation of Nu_q with density ratio at different radiation intensities and at fixed $Ra = 10^7$ in figures 6(*a*,*b*). Despite the small difference in magnitudes, it is noted that the variation of Nu_q with density ratio is similar for 2-D cases and 3-D cases. As the density ratio is increased, Nu_q decreases very rapidly at first, and then slowly becomes less than 0. This indicates that the small-density-ratio particles can absorb more radiation heat and then transfer relatively more heat to the fluid, as the settling of small-density-ratio particles is slow. It is also noted that particles with a large density ratio always absorb heat from fluid even at very large radiation intensity $\phi = 100 \times \phi_{solar}$, as the temperature of particles is increased a little under the process of fast settling. Two different regimes can be identified: the exothermal particle regime where Nu_q is larger than 0, and the endothermal particle regime where Nu_q is less than 0. The division between the two regimes gives a critical density ratio ρ_c/ρ_0 at which Nu_q crosses 0. The regime shifts towards larger ρ_p/ρ_0 when the radiation intensity is increased, suggesting that the exothermal particle regime occurs more easily at larger radiation intensity. To better compare the Nu_q values at different radiation intensities, we adopt ρ_c/ρ_0 and the single-phase Nusselt number Nu^* to normalize the data, and the results are plotted in figures 6(*c*,*d*). It is seen that all symbols can collapse on a curve for both 2-D and 3-D cases. The two curves can be well described

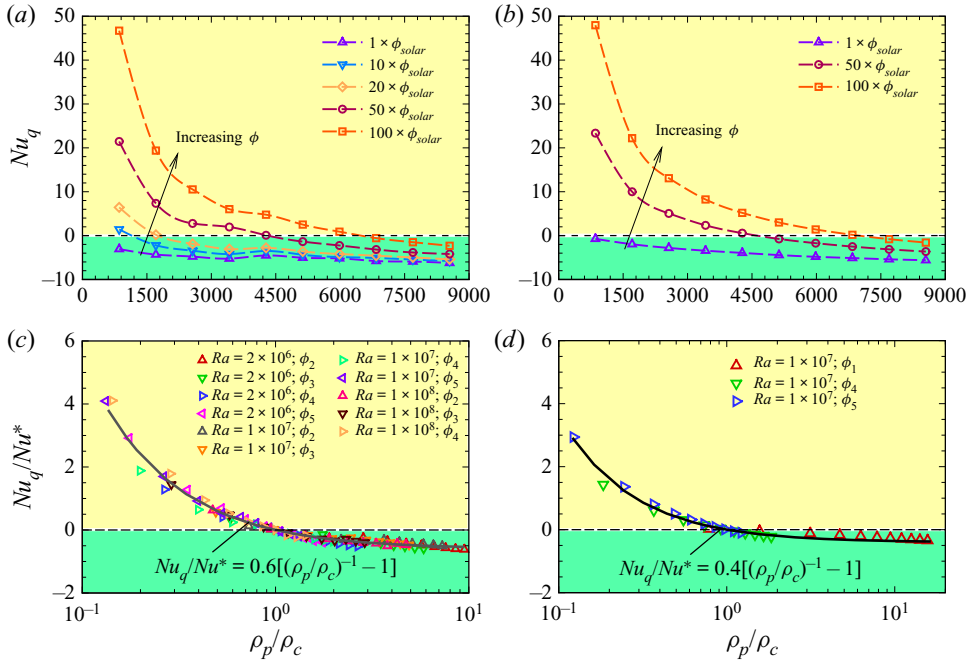

Figure 6. Plots of Nu_q as a function of ρ_p/ρ_0 obtained at various ϕ and fixed $Ra = 10^7$ for (*a*) 2-D cases and (*b*) 3-D cases. Ratio Nu_q/Nu^* as a function of the normalized density ratio ρ_p/ρ_c for (*c*) all 2-D cases and (*d*) all 3-D cases; the black solid curves are the best power function fits to the respective data. Here, ϕ_1, ϕ_2, ϕ_3, ϕ_4 and ϕ_5 represent the radiation strengths of ϕ_{solar}, $10\phi_{solar}$, $20\phi_{solar}$, $50\phi_{solar}$ and $100\phi_{solar}$, respectively.

by $Nu_q/Nu^* = C_q[(\rho_p/\rho_c)^{-1} - 1]$, where the constant parameter C_q equals 0.6 for the 2-D simulations, and 0.4 for the 3-D simulations. This indicates that ρ_c/ρ_0 is indeed a relevant typical density ratio for the problem. This signals that the interphase heat transfers for all cases studied exhibit universal properties and are governed by the same transfer mechanism. In addition, Nu_q values increase linearly with the radiation intensity, and their slopes become large as the density ratio decreases, as shown in figure 7(*a*). Here, α is the growth rate of Nu_q with radiation intensity. In figure 7(*b*), we summarize α in the best linear relation fits of $Nu_q \sim \alpha(\phi/\phi_{solar})$ as a function of the density ratio and the Rayleigh number. One sees that all data collapse onto a single curve, and the best power-law fits to the data yield $\alpha \sim (\rho_p/\rho_0)^{-1.11}\, Ra^{0.65}$.

3.4. *The energy transport*

We plot the schematic of the energy process in the particle-laden RB convection as shown in figure 8. In this flow system, the fluid energy includes kinetic energy and thermal energy. Fluid kinetic energy can be obtained through interaction between thermal buoyancy or particle and fluid, and finally dissipated by fluid viscosity. The injected kinetic energy is from the work done by the driving buoyancy and the momentum feedback of particles $\boldsymbol{F}\cdot\boldsymbol{u}$; the injected thermal energy includes the part of the heat flux from the hot/cold plate and the thermal feedback of particles QT. The energy finally dissipates due to the fluid viscosity and the thermal diffusivity.

The kinetic energy of the fluid in RB convection can be revealed by the Reynolds number, as shown in figure 4 and discussed in § 3.2. For the 2-D cases, the particle-induced

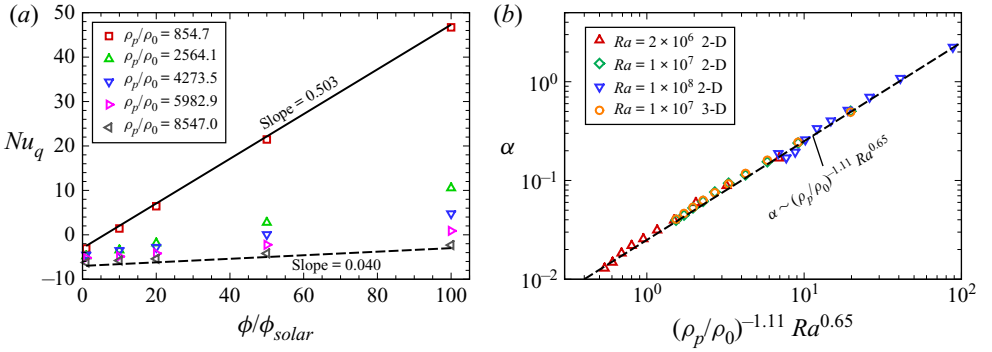

Figure 7. (*a*) Plots of Nu_q as functions of ϕ/ϕ_{solar} obtained at various density ratios ρ_p/ρ_0 and fixed $Ra = 10^7$ for 2-D cases. The solid and dashed lines are eye guides. (*b*) Fitted slope in the linear relation $Nu_q \sim \alpha(\phi/\phi_{solar})$ as a function of the product $(\rho_p/\rho_0)^{-1.11}\, Ra^{0.65}$ for both 2-D and 3-D cases. The black dashed line is the fitted relation for α versus $(\rho_p/\rho_0)^{-1.11}\, Ra^{0.65}$.

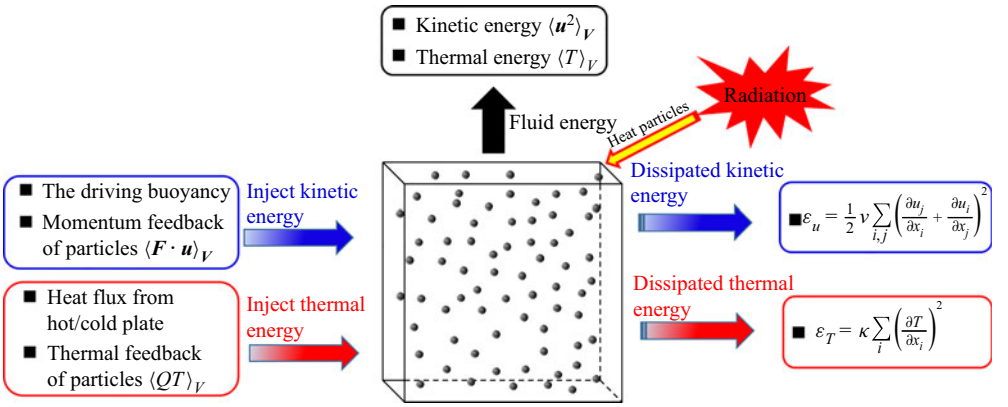

Figure 8. The schematic of the energy process in the RB convection laden with heated particles.

kinetic energy $\langle \boldsymbol{F} \cdot \boldsymbol{u} \rangle_{V,t}$ is important for a small-density-ratio particle, as shown in figure 9(*a*). Our recent work revealed that the mechanism for the increased *Re* as shown in figure 4(*a*) results from particle-induced kinetic energy, therefore it enhances the strength of turbulence (Yang *et al.* 2022*b*). For the 3-D cases, the particle-induced kinetic energy decreases with the increasing of ρ_p/ρ_0, while the fluid kinetic energy increases at larger ρ_p/ρ_0. This implies that the thermal plumes shed from heated particles accelerate the motion of flow eddies, and its contribution to the fluid is larger than that of particle-induced kinetic energy. That explains why the alteration of fluid kinetic energy is dominated by the particle-induced kinetic energy for the 2-D cases, while it is dominated by the buoyancy-induced kinetic energy by the heated particles for the 3-D cases.

The volume-averaged temperature of the fluid can reflect the fluid thermal energy; figure 10 shows the volume-averaged temperature $\langle T \rangle_{V,t}$ of the fluid as functions of ρ_p/ρ_0 at fixed $Ra = 10^7$. Despite the different magnitudes, both the data sets exhibit a similar trend with Nu_q, i.e. $\langle T \rangle_{V,t}$ decreases with increasing ρ_p/ρ_0, and reaches a value less than the single-phase temperature, for both the 2-D and 3-D cases. The $\langle T \rangle_{V,t}$ value tends to be larger for large radiation intensity. Notably, the $\langle T \rangle_{V,t}$ value of the 3-D simulations

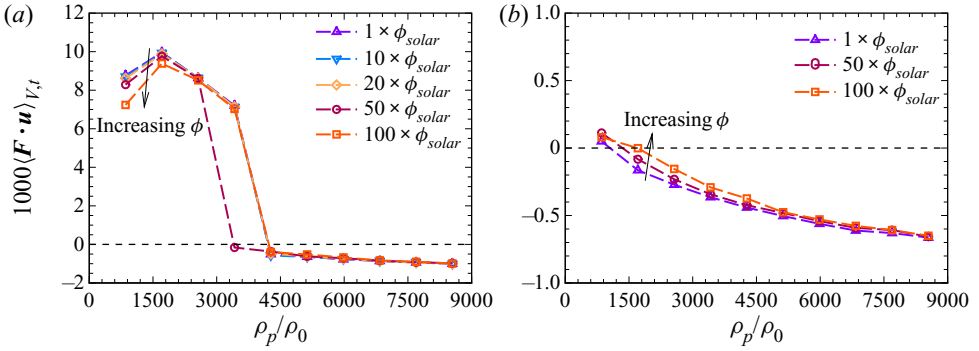

Figure 9. The particle-induced kinetic energy as functions of ρ_p/ρ_0 obtained at various ϕ and fixed $Ra = 10^7$ for (*a*) 2-D cases and (*b*) 3-D cases.

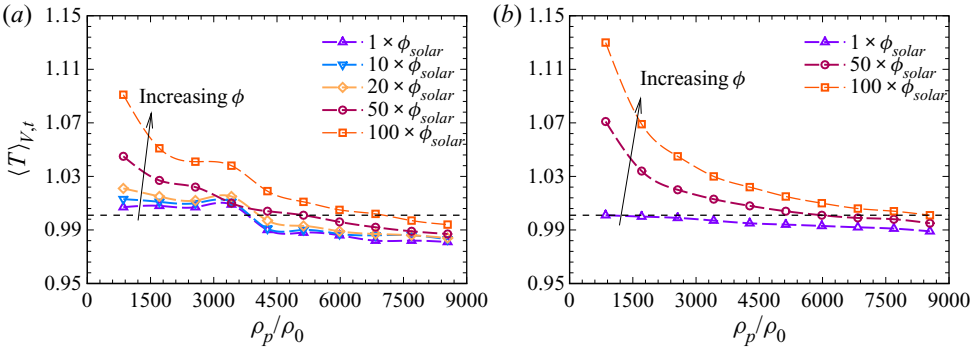

Figure 10. The volume-averaged temperature as functions of ρ_p/ρ_0 obtained at various ϕ and fixed $Ra = 10^7$ for (*a*) 2-D cases and (*b*) 3-D cases.

is significantly larger than that of 2-D simulations at small ρ_p/ρ_0 for large radiation intensities $\phi = 50 \times \phi_{solar}$ and $100 \times \phi_{solar}$, even if there is little difference Nu_q between the 2-D and 3-D simulations, as shown in figure 6. This implies that Nu_q is an important reference quantity for fluid heating, but it is not the only factor. It also involves the dynamics of RB turbulent convection.

The particle-induced thermal energy is described by $\langle Q\rangle_{V,t}$, and we plot $\langle QT\rangle_{V,t}$ as functions of ρ_p/ρ_0 at fixed $Ra = 10^7$ and at different radiation intensities, as shown in figures 11(*a*,*b*). Here, $\langle QT\rangle_{V,t}$ and Nu_q have similar trends as functions of ρ_p/ρ_0 at different radiation intensities. Namely, with increasing ρ_p/ρ_0, $\langle QT\rangle_{V,t}$ decreases rapidly at first, and then decreases slowly below 0. The particles with small ρ_p/ρ_0 can transport more thermal energy to the fluid. The exothermal particle regime and endothermal particle regime are also observed, and the critical density ratio ρ_c/ρ_0 between the two regimes is the same as that of Nu_q for specific radiation intensity. This implies that the interphase heat transfer mechanism is consistent with the interphase thermal energy transport mechanism. We further rescale $\langle QT\rangle_{V,t}$ by the thermal dissipation rate of the single-phase case, and ρ_p/ρ_0 by the critical density ratio ρ_c/ρ_0, as shown in figures 11(*c*,*d*). This rescaling leads to the converging of the data onto a single curve for 2-D and 3-D cases, representing the functions $\langle QT\rangle_{V,t}/\langle\varepsilon_T^*\rangle_{V,t} = C_{qt}[(\rho_p/\rho_c)^{-1} - 1]$ with the constant equal to 4.5 and 3.0 for the 2-D and 3-D cases, respectively, where the thermal dissipation rate of single-phase is

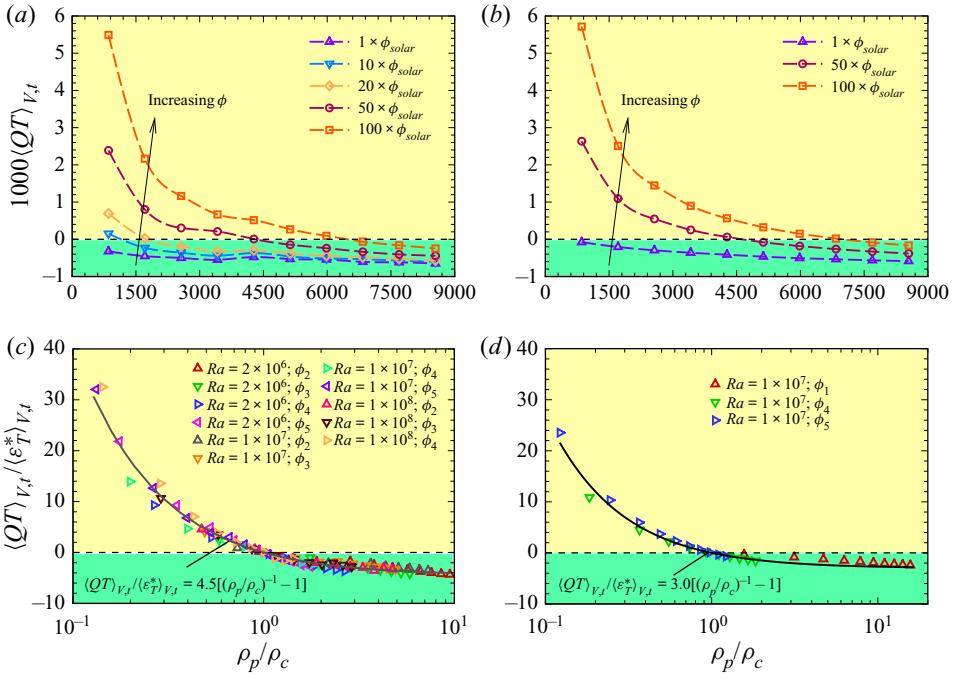

Figure 11. The particle-to-fluid thermal energy $\langle QT\rangle_{V,t}$ as a function of ρ_p/ρ_0 obtained at various ϕ and fixed $Ra = 10^7$ for (*a*) 2-D cases and (*b*) 3-D cases. Ratio $\langle QT\rangle_{V,t}/\langle\varepsilon_T^*\rangle_{V,t}$ as a function of the normalized density ratio ρ_p/ρ_c for (*c*) all 2-D cases and (*d*) all 3-D cases; the black solid curves are the best power function fits to the respective data. Here, ϕ_1, ϕ_2, ϕ_3, ϕ_4 and ϕ_5 represent the radiation strengths of ϕ_{solar}, $10\phi_{solar}$, $20\phi_{solar}$, $50\phi_{solar}$ and $100\phi_{solar}$, respectively.

expressed as $\varepsilon_T^* = 1/(Ra\,Pr)^{1/2}k\sum_i(\partial T/\partial x_i)^2$. Moreover, $\langle QT\rangle_{V,t}$ increases linearly with increasing radiation intensity at different density ratios ρ_p/ρ_0. The linear slope increases with the decrease of the density ratio ρ_p/ρ_0, as shown in figure 12(*a*). Figure 12(*b*) plots the growth rate β of particle-induced thermal energy with radiation intensity in the linear relation $1000\langle QT\rangle_{V,t} \sim \beta(\phi/\phi_{solar})$ at various Ra and ρ_p/ρ_0. One sees that all growth rates converge onto a curve, and the scaling relation of growth rate β versus Rayleigh number and density ratio can be obtained, i.e. $\beta \sim (\rho_p/\rho_0)^{-1.20}\,Ra^{0.18}$.

3.5. *The critical density ratio*

It is noted that there are two regimes, i.e. the exothermal particle regime and the endothermal particle regime; a critical density ratio divides the two regimes, at which both Nu_q and $\langle QT\rangle_{V,t}$ equal 0. The critical density is crucial for the interphase heat transfer and thermal energy transport. The critical density ratios ρ_p/ρ_c as functions of radiation intensity and Rayleigh number are illustrated in figures 13(*a*,*b*). One sees that the critical density ratio ρ_p/ρ_c of 2-D cases collapses onto a single curve that is well described by the power law $\rho_p/\rho_c \sim (\phi/\phi_{solar})^{3/4}\,Ra^{0.18}$. For the 3-D cases, the critical density ratio is larger than that of the 2-D cases at the present radiation intensity, as shown in figures 6(*a*,*b*). Nevertheless, the $\rho_p/\rho_c - (\phi/\phi_{solar})$ data set approaches the scaling of $\rho_p/\rho_c \sim (\phi/\phi_{solar})^{0.55}$, which is not as steep as the 2-D cases.

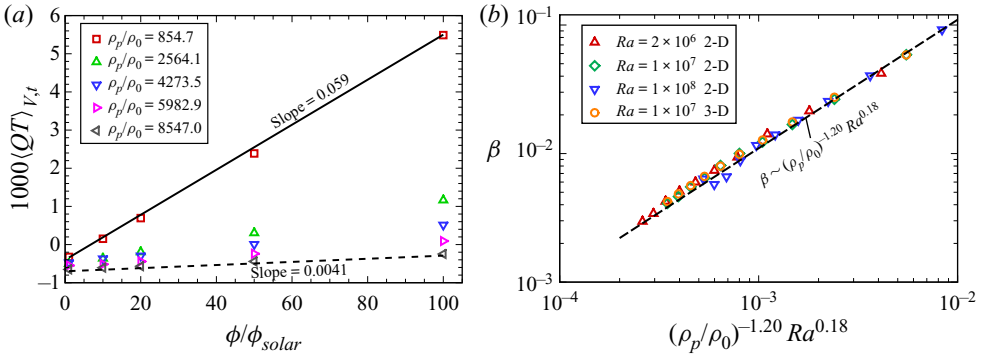

Figure 12. (*a*) Plots of $\langle QT\rangle_{V,t}$ as functions of ϕ/ϕ_{solar} obtained at various density ratios ρ_p/ρ_0 and fixed $Ra = 10^7$ for 2-D cases. The solid and dashed lines are eye guides. (*b*) Fitted slope in the linear relation $1000\langle QT\rangle_{V,t} \sim \beta(\phi/\phi_{solar})$ as a function of the product $(\rho_p/\rho_0)^{-1.2}\, Ra^{0.18}$ for both 2-D and 3-D cases. The black dashed line is the fitted relation for β versus $(\rho_p/\rho_0)^{-1.2}\, Ra^{0.18}$.

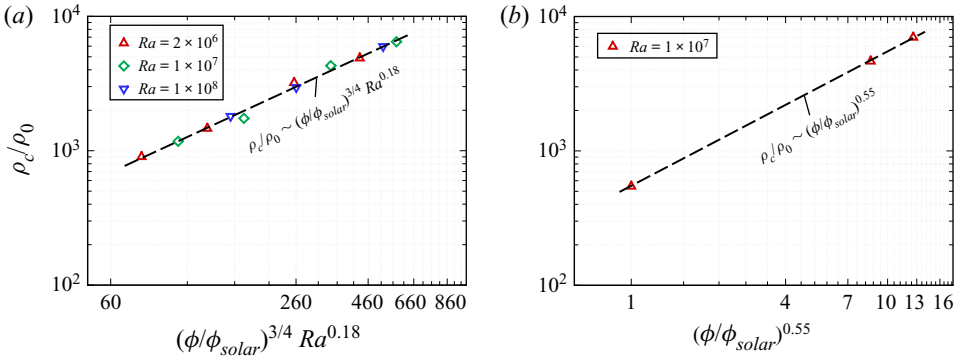

Figure 13. (*a*) The characteristic density ratio ρ_p/ρ_0 as a function of the product $(\phi/\phi_{solar})^{3/4}\, Ra^{0.18}$ for all the 2-D cases. (*b*) The characteristic density ratio ρ_p/ρ_0 as a function of the product $(\phi/\phi_{solar})^{0.55}$ for all the 3-D cases. The black dashed lines are the best functions that fit the respective data.

To deeply understand the above dependencies, we first idealize the scene for the critical-density particle-laden cases as the situation where the temperature of particles is consistently equal to the local fluid temperature during the settling of particles; particles settle directly towards the bottom plate and are not advected into the bulk region again. Based on this, the particle thermal equation is

$$\frac{\mathrm{d}T_p}{\mathrm{d}t} = \frac{Nu_p}{2}\,\frac{T_f - T_p}{St_T} + q. \tag{3.9}$$

According to the above approximation, the first term of the right-hand side vanishes, so

$$\frac{\mathrm{d}T_p}{\mathrm{d}t} = q. \tag{3.10}$$

We integrate both sides of (3.10) from t_1 to t_2 for a specific particle, where the particle is released from the top plate at t_1 and reaches the bottom plate at t_2. According to the

boundary condition of the convection cell, we can get

$$\frac{T_p(t_2) - T_p(t_1)}{t_2 - t_1} = \frac{2\varepsilon}{1/S_p} = q, \tag{3.11}$$

where S_p is the averaged settling velocity of particles. Additionally, we give the formulation of q as

$$q = \frac{(\pi/4)d_p^2\phi}{c_{p,p}m_pT_0/(H/(2\varepsilon g))^{1/2}}, \tag{3.12}$$

reforming it to get

$$q = \frac{3}{2}\frac{\phi}{\phi_{solar}}\left(\frac{c_{p,p}}{c_{p,0}}\frac{\rho_c}{\rho_0}\frac{d_p}{H}\right)^{-1}\frac{\phi_{solar}}{k_0T_0/H}(Ra\,Pr)^{-1/2}. \tag{3.13}$$

According to Yang *et al.* (2022*b*), $S_p \simeq \frac{1}{18}(1/Fr_p^2)(\rho_c/\rho_0)(d_p^2/H^2)(Ra/Pr)^{1/2}$ in the RB convection. Consequently, for the cases with critical density, we can get that

$$\left(\frac{\rho_c}{\rho_0}\right)^2 \sim \frac{Fr_p^2}{2\varepsilon}\frac{\phi}{\phi_{solar}}\frac{\phi_{solar}}{k_0T_0/H}\left(\frac{d_p}{H}\right)^{-3}\left(\frac{c_{p,p}}{c_{p,0}}\right)^{-1}Ra^{-1}. \tag{3.14}$$

In the present study, the non-dimensional temperature difference ε between the top and bottom plates is constant. Also, the working fluid is air at 300 K, and the physical properties are also constant. Based on these facts, we can get $H \sim Ra^{1/3}$, and consequently

$$\frac{\rho_c}{\rho_0} \sim \left(\frac{\phi}{\phi_{solar}}\right)^{1/2}Ra^{1/3}. \tag{3.15}$$

On account of the approximate assumption and the simplification in the derivative procedure, there are three causes that can result in a small adjustment in the scaling exponent for (3.15):

(1) In real turbulent circumstances, the transport modes of particles are complex and diverse due to the interaction between turbulence and particles, and the particles near the bottom plate can be brought into the bulk again by the fluid.
(2) The temperature of particles would not be consistently equal to the local fluid temperature during the settling of particles.
(3) The kinetic and dynamic behaviour of particles in turbulence can result in some small adjustments for the expression of particle settling velocity S_p, according to the discussion of Yang *et al.* (2022*b*).

Specifically, for the 2-D cases, the scaling relation $\rho_c/\rho_0 \sim (\phi/\phi_{solar})^{3/4}\,Ra^{0.18}$ of the computed data has relative large difference with the derived scaling $\rho_c/\rho_0 \sim (\phi/\phi_{solar})^{1/2}\,Ra^{1/3}$ on account of the transport modes of particles being diverse and not as simple as the simplification. For the 3-D cases, the derived scaling $\rho_c/\rho_0 \sim (\phi/\phi_{solar})^{1/2}$ is very close to the obtained scaling relation $\rho_c/\rho_0 \sim (\phi/\phi_{solar})^{0.55}$ from computed data as the transport of particles is similar to the approximation. What is more, we predict the critical density ratio to be $\rho_c/\rho_0 = 2155.48$ for $\phi/\phi_{solar} = 50$ at $Ra = 10^6$ and $Pr = 0.71$ by using the scaling $\rho_c/\rho_0 \sim (\phi/\phi_{solar})^{0.55}\,Ra^{1/3}$, and the computed result shows $Nu_q = 0.848$, which is close to 0; this shows that the predicted critical density ratio is very close to the real critical density ratio. This indicates that the theoretically predicted scaling can well describe the relation between the critical density ratio and the control parameters for the 3-D cases.

4. Conclusion

We carried out the DNS combined with the Lagrangian point-particle mode for the RB convection laden with heated inertial particles, where the two-phase flow is relevant to particle-based solar receivers. We consider the particle–turbulence system in the ranges of density ratio $854.7 \leq \rho_p/\rho_0 \leq 8547$ and radiation intensity $1 \leq \phi/\phi_{solar} \leq 100$ for 2-D and 3-D simulations. Three Rayleigh numbers, $Ra = 2 \times 10^6$, 1×10^7 and 1×10^8 are considered for 2-D simulations, and $Ra = 1 \times 10^7$ is considered for 3-D simulations at fixed $Pr = 0.71$. We also theoretically derive and analyse the exact relation for the interphase heat transfer in the heated particle-laden RB convection, which shows that the Nusselt number difference between the cold and hot plates is caused by the interphase heat transfer in the cell.

We found that particles with small density ratio and encountering strong radiation significantly alter the flow momentum transport and fluid heat transfer, especially enhancing the top plate heat transport, so the fluid temperature of the bulk is remarkably heated. This indicates that the small-density-ratio particles absorb more radiant heat in the slow settlement process, which further leads to the increase of heat flux between the top plate and particles. Also, the heat transfer of the bottom plate becomes small at a small density ratio, and the heat flux changes from positive to negative, and increases gradually under the high radiation intensity. The negative value of heat transfer means that the direction of heat flux is from up to down; this is because the temperature of particles is significant higher than that of the bottom plate. Due to the preferential sweeping of particles, particle clusters are relevant to the edges of eddies at small density ratio for the 2-D cases, where particles can effectively do work on these eddies; this significantly enhances the momentum transport of fluid.

What is more, two different regimes are observed: the exothermal particle regime and the endothermal particle regime. By using the critical density ratio, the Nusselt number and the energy dissipation rate of the single-phase flow as characteristic quantities to normalize the data, both the interphase heat transfer and the interphase thermal energy transport exhibit universal properties that are governed by the specific transfer mechanism, respectively. They can be well described by $Nu_q/Nu^* = C_q[(\rho_p/\rho_c)^{-1} - 1]$ and $\langle QT\rangle_{V,t}/\langle\varepsilon_T^*\rangle_{V,t} = C_{qt}[(\rho_p/\rho_c)^{-1} - 1]$, respectively, where the constant parameter C_q equals 0.6 for the 2-D simulations and 0.4 for the 3-D simulations, and with the constant C_{qt} equal to 4.5 and 3.0 for the 2-D and 3-D cases, respectively. Additionally, both the interphase heat transfer and the interphase thermal energy transport also increase linearly with the increasing of radiation intensity. The linear growth rates in $Nu_q \sim \alpha(\phi/\phi_{solar})$ and $1000\langle QT\rangle_{V,t} \sim \beta(\phi/\phi_{solar})$ exhibit the scaling relations $\alpha \sim (\rho_p/\rho_0)^{-1.11}\, Ra^{0.65}$ and $\beta \sim (\rho_p/\rho_0)^{-1.20}\, Ra^{0.18}$, respectively.

Finally, the critical density ratios where the two regimes are divided are the same for both the interphase heat transfer and the interphase thermal energy transport at specific radiation intensity. The scaling relations of critical density ratio versus radiation intensity and Rayleigh number are described by the power law $\rho_p/\rho_c \sim (\phi/\phi_{solar})^{3/4}\, Ra^{0.18}$ for the 2-D cases, and $\rho_p/\rho_c \sim (\phi/\phi_{solar})^{0.55}\, Ra^{\gamma}$ for the 3-D simulations. We further predict theoretically the power-law relation of the critical density ratios versus Rayleigh number and radiation intensity, i.e. $\rho_p/\rho_c \sim (\phi/\phi_{solar})^{1/2} Ra^{1/3}$, which is in remarkable agreement with our 3-D simulations.

Funding. This work was supported by the Natural Science Foundation of China (grant nos 12172207, 92052201 and 11825204), and the Shanghai Science and Technology Program under project no. 19JC1412802.

Declaration of interests. The authors report no conflict of interest.

Author ORCIDs.
Wenwu Yang https://orcid.org/0000-0002-1671-7431;
Zhen-Hua Wan https://orcid.org/0000-0003-0035-3116;
Quan Zhou https://orcid.org/0000-0002-0411-7228;
Yuhong Dong https://orcid.org/0000-0002-9332-9870.

References

Ahlers, G., Grossmann, S. & Lohse, D. 2009 Heat transfer and large scale dynamics in turbulent Rayleigh–Bénard convection. *Rev. Mod. Phys.* **81**, 503–537.

Ahmed, A.M. & Elghobashi, S. 2000 On the mechanisms of modifying the structure of turbulent homogeneous shear flows by dispersed particles. *Phys. Fluids* **12** (11), 2906–2930.

Balachandar, S. & Eaton, J.K. 2010 Turbulent dispersed multiphase flow. *Annu. Rev. Fluid Mech.* **42**, 111–133.

Banko, A.J., Villafñe, L., Kim, J.H. & Eaton, J.K. 2020 Temperature statistics in a radiatively heated particle-laden turbulent square duct flow. *Intl J. Heat Fluid Flow* **84**, 108618.

Bec, J., Homann, H. & Ray, S.S. 2014 Gravity-driven enhancement of heavy particle clustering in turbulent flow. *Phy. Rev. Lett.* **112** (18), 184501.

Boivin, M., Simonin, O. & Squires, K.D. 1998 Direct numerical simulation of turbulence modulation by particles in isotropic turbulence. *J. Fluid Mech.* **375**, 235–263.

Bosse, T., Kleiser, L. & Meiburg, E. 2006 Small particles in homogeneous turbulence: settling velocity enhancement by two-way coupling. *Phys. Fluids* **18**, 027102.

Boussinesq, J. 1903 *Theorie Analytique de la Chaleur*, vol. 2. Gauthier-Villars.

Bragg, A.D., Richter, D.H. & Wang, G. 2021 Mechanisms governing the settling velocities and spatial distributions of inertial particles in wall-bounded turbulence. *Phys. Rev. Fluids* **6**, 064302.

Briggs, W.L., Henson, V.E. & McCormick, S.F. 2000 *A Multigrid Tutorial*, vol. 72. SIAM.

Carbone, M., Bragg, A.D. & Iovieno, M. 2019 Multiscale fluid–particle thermal interaction in isotropic turbulence. *J. Fluid Mech.* **881**, 679–721.

Chen, H., Chen, Y., Hsieh, H.-T. & Siegel, N. 2007 Computational fluid dynamics modeling of gas-particle flow within a solid-particle solar receiver. *J. Sol. Energy Engng* **129** (2), 160–170.

Cherukat, P., Mclaughlin, J.B. & Dandy, D.S. 1998 A computational study of the inertial lift on a sphere in a linear shear flow field. *Intl J. Multiphase Flow* **25**, 15–33.

Chillà, F. & Schumacher, J. 2012 New perspectives in turbulent Rayleigh–Bénard convection. *Eur. Phys. J.* E **35** (7), 58.

Chinnici, A., Arjomanidi, M., Tian, Z.F., Lu, Z. & Nathan, G.J. 2015 A novel solar expanding-vortex particle reactor: influence of vortex structure on particle residence times and trajectories. *Solar Energy* **122**, 58–75.

Chung, J.N. & Troutt, T.R. 1988 Simulation of particle dispersion in an axisymmetric jet. *J. Fluid Mech.* **186**, 199–222.

Crowe, C.T. 1982 Review: numerical models for dilute gas-particle flows. *Trans. ASME J. Fluids Engng* **104**, 297–303.

Crowe, C.T., Gore, R. & Troutt, T.R. 1985 Particles dispersion by coherent structures in free shear flows. *Particul. Sci. Tech.* **3**, 149–158.

Crowe, C.T., Troutt, T.R. & Chung, J.N. 1996 Numerical models for two-phase turbulent flows. *Annu. Rev. Fluid Mech.* **28**, 11–43.

Davis, D., Jafarian, M., Chinnici, A., Saw, W.L. & Nathan, G.J. 2019 Thermal performance of vortex-based solar particle receiver for sensible heating. *Solar Energy* **177**, 163–177.

Dong, Y. & Chen, L. 2011 The effect of stable stratification and thermophoresis on fine particle deposition in a bounded turbulent flow. *Intl J. Heat Mass Transfer* **54**, 1168–1178.

Druzhinin, O.A. & Elghobashi, S. 1999 On the decay rate of isotropic turbulence laden with microparticles. *Phys. Fluids* **11** (3), 602–610.

Elghobashi, S. 1991 Particle-laden turbulent flows: direct simulation and closure models. *Appl. Sci. Res.* **48**, 301–314.

Elghobashi, S. 1994 On predicting particle-laden turbulent flows. *Appl. Sci. Res.* **52**, 309–329.

Elghobashi, S. 2019 Direct numerical simulation of turbulent flows laden with droplets or bubbles. *Annu. Rev. Fluid Mech.* **51**, 217–244.

ELGHOBASHI, S. & TRUESDELL, G.C. 1992 Direct simulation of particle dispersion in a decaying isotropic turbulence. *J. Fluid Mech.* **242**, 655–700.

ELGHOBASHI, S. & TRUESDELL, G.C. 1993 On the two-way interaction between homogeneous turbulence and dispersed solid particles. I. Turbulence modification. *Phys. Fluids* A **5** (7), 1790–1801.

FERRANTE, A. & ELGHOBASHI, S. 2003 On the physical mechanisms of two-way coupling in particle-laden isotropic turbulence. *Phys. Fluids* **15** (2), 315–329.

FRANKEL, A., IACCARINO, G. & MANI, A. 2017 Optical depth in particle-laden turbulent flows. *J. Quant. Spectrosc. Radiat. Transfer* **201**, 10–16.

FRANKEL, A., POURANSARI, H., COLETTI, F. & MANI, A. 2016 Settling of heated particles in homogeneous turbulence. *J. Fluid Mech.* **792**, 869–893.

GERELTBYAMBA, B. & LEE, C. 2019 Flow modification by inertial particles in a differentially heated cubic cavity. *Intl J. Heat Fluid Flow* **78**, 108445.

GOOD, G., GERASHCHENKO, S. & WARHAFT, Z. 2012 Intermittency and inertial particle entrainment at a turbulent interface: the effect of the large-scale eddies. *J. Fluid Mech.* **694**, 371–398.

GRABOWSKI, W.W. & WANG, L.-P. 2013 Growth of cloud droplets in a turbulent environment. *Annu. Rev. Fluid Mech.* **45**, 293–324.

GROSSMANN, S. & LOHSE, D. 2000 Scaling in thermal convection: a unifying theory. *J. Fluid Mech.* **407**, 27–56.

GUHA, A. 2008 Transport and deposition of particles in turbulent and laminar flow. *Annu. Rev. Fluid Mech.* **40**, 311–341.

HANNA, S.R. 1969 The formation of longitudinal sand dunes by large helical eddies in the atmosphere. *J. Appl. Meteorol.* **8** (6), 874–883.

HO, C.K. 2016 A review of high-temperature particle receivers for concentrating solar power. *Appl. Therm. Engng* **109** (B), 958–969.

HUANG, S.-D., KACZOROWSKI, M., NI, R. & XIA, K.-Q. 2013 Confinement-induced heat-transport enhancement in turbulent thermal convection. *Phys. Rev. Lett.* **111**, 104501.

HUNT, J.C.R. 1991 Industrial and environmental fluid mechanics. *Annu. Rev. Fluid Mech.* **23**, 1–41.

IRELAND, P.J., BRAGG, A.D. & COLLINS, L.R. 2016 The effect of Reynolds number on inertial particle dynamics in isotropic turbulence. Part 1. Simulations without gravitational effects. *J. Fluid Mech.* **796**, 617–658.

JELLINEK, A.M. & KERR, R.C. 2001 Magma dynamics, crystallization, and chemical differentiation of the 1959 Kilauea Iki lava lake, Hawaii, revisited. *J. Volcanol. Geotherm. Res.* **110**, 235–263.

KIM, K., SIEGEL, N., KOLB, G., RANGASWAMY, V. & MOUJAES, S.F. 2009 A study of solid particle flow characterization in solar particle receiver. *Solar Energy* **83**, 1784–1793.

KOK, J.F., PARTELI, E.J., MICHAELS, T.I. & KARAM, D.B. 2012 The physics of wind-blown sand and dust. *Rep. Prog. Phys.* **75**, 106901.

KRAICHNAN, R.H. 1967 Inertial ranges in two-dimensional turbulence. *Phys. Fluids* **10** (7), 1417–1423.

KULICK, J.D., FESSLER, J.R. & EATON, J.K. 1994 Particle response and turbulence modification in fully developed channel flow. *J. Fluid Mech.* **277** (1), 109–134.

KUROSE, R. & KOMORI, S. 1999 Drag and lift forces on a rotating sphere in a linear shear flow. *J. Fluid Mech.* **384**, 183–206.

LANDAU, L.D. & LIFSHITZ, E.M. 1987 *Fluid Mechanics*. Pergamon.

LÁZARO, B.J. & LASHERAS, J.C. 1992 Particle dispersion in the developing free shear layer. Part 2. Forced flow. *J. Fluid Mech.* **235**, 179–211.

LIU, C., TANG, S., DONG, Y. & SHEN, L. 2018 Heat transfer modulation by inertial particles in particle-laden turbulent channel flow. *Trans. ASME J. Heat Transfer* **140** (11), 112003.

LIU, S., XIA, S.-N., YAN, R., WAN, Z.-H. & SUN, D.-J. 2018 Linear and weakly nonlinear analysis of Rayleigh–Bénard convection of perfect gas with non-Oberbeck–Boussinesq effects. *J. Fluid Mech.* **845**, 141–169.

LOHSE, D. & XIA, K.-Q. 2010 Small-scale properties of turbulent Rayleigh–Bénard convection. *Annu. Rev. Fluid Mech.* **42**, 335–364.

LONGMIRE, E.K. & EATON, J.K. 1992 Structure of a particle-laden round jet. *J. Fluid Mech.* **236**, 217–257.

LOTH, E. 2000 Numerical approaches for motion of dispersed particles, droplets and bubbles. *Prog. Energy Combust. Sci.* **26**, 161–223.

MAXEY, M.R. 1987 The gravitational settling of aerosol particles in homogeneous turbulence and random flow fields. *J. Fluid Mech.* **174**, 441–465.

MAXEY, M.R. & CORRSIN, S. 1986 Gravitational settling of aerosol particles in randomly oriented cellular flow fields. *J. Atmos. Sci.* **43**, 1112–1134.

MEI, R. 1992 An approximate expression for the shear lift force on a spherical particle at finite Reynolds number. *Intl J. Multiphase Flow* **18**, 145–147.

MOMENIFAR, M. & BRAGG, A.D. 2020 Local analysis of the clustering, velocities and accelerations of particles settling in turbulence. *Phys. Rev. Fluids* **5**, 034306.

MONCHAUX, R., BOURGOIN, M. & CARTELLIER, A. 2010 Preferential concentration of heavy particles: a Voronoï analysis. *Phys. Fluids* **22**, 1112–1134.

NIELSEN, P. 1993 Turbulence effects on the settling of suspended particles. *J. Sedim. Petrol.* **63**, 835–838.

ORESTA, P. & PROSPERETTI, A. 2013 Effects of particle settling on Rayleigh–Bénard convection. *Phys. Rev.* E **87**, 063014.

PAOLUCCI, S. 1982 Filtering of sound from the Navier–Stokes equations. *NASA STI Tech. Rep.* Recon Tech. Rep. N, 83, 26036.

PARK, H.J., O'KEEFE, K. & RICHTER, D.H. 2018 Rayleigh–Bénard turbulence modified by two-way coupled inertial, nonisothermal particles. *Phys. Rev. Fluids* **3**, 034307.

PATOČKA, V., CALZAVARINI, E. & TOSI, N. 2020 Settling of inertial particles in turbulent Rayleigh–Bénard convection. *Phys. Rev. Fluids* **5**, 114304.

VAN DER POEL, E.P., STEVENS, R.J. & LOHSE, D. 2013 Comparison between two- and three-dimensional Rayleigh–Bénard convection. *J. Fluid Mech.* **736**, 117–197.

POURANSARI, H. & MANI, A. 2017 Effects of preferential concentration on heat transfer in particle-based solar receivers. *J. Solar Energy Engng* **139**, 021008.

POURANSARI, H. & MANI, A. 2018 Particle-to-fluid heat transfer in particle-laden turbulence. *Phys. Rev. Fluids* **3**, 074304.

PURAGLIESI, R., DEHBI, A., LERICHE, E., SOLDATI, A. & DEVILLE, M.O. 2011 DNS of buoyancy-driven flows and Lagrangian particle tracking in a square cavity at high Rayleigh numbers. *Intl J. Heat Fluid Flow* **32**, 915–931.

RAHMANI, M., GERACI, G., IACCARINO, G. & MANI, A. 2018 Effects of particle polydispersity on radiative heat transfer in particle-laden turbulent flows. *Intl J. Multiphase FLow* **104**, 42–59.

RANZ, W. & MARSHALL, W. 1952 Evaporation from drops. *Chem. Engng Prog.* **48**, 142–180.

REEKS, M.W. 1983 The transport of discrete particles in inhomogeneous turbulence. *J. Aerosol Sci.* **14**, 729–739.

SAFFMAN, P.G. 1965 The lift on a small sphere in a slow shear flow. *J. Fluid Mech.* **22**, 385–400.

SAHU, S., HARDALUPAS, Y. & TAYLER, A.M.K.P. 2014 Droplet–turbulence interaction in a confined polydispersed spray: effect of droplet size and flow length scales on spatial droplet–gas velocity correlations. *J. Fluid Mech.* **741**, 98–138.

SHAW, R.A. 2003 Particle–turbulence interactions in atmospheric clouds. *Annu. Rev. Fluid Mech.* **35**, 183–227.

SHOTORBAN, B., MASHAYEK, F. & PANDYA, R. 2003 Temperature statistics in particle-laden turbulent homogeneous shear flow. *Intl J. Multiphase Flow* **29** (8), 117–153.

SHRAIMAN, B.I. & SIGGIA, E.D. 1990 Heat transport in high-Rayleigh number convection. *Phys. Rev.* A **43**, 3650–3653.

SIGGIA, E.D. 1994 High Rayleigh number convection. *Annu. Rev. Fluid Mech.* A **26**, 137–168.

SQUIRES, K.D. & EATON, J.K. 1991 Preferential concentration of particles by turbulence. *Phys. Fluids* **3**, 1989–1993.

STEVENS, R.J.A.M., VERZICCO, R. & LOHSE, D. 2010 Radial boundary layer structure and Nusselt number in Rayleigh–Bénard convection. *J. Fluid Mech.* **643**, 495–507.

SUSLOV, S.A. 2010 Mechanism of nonlinear flow pattern selection in moderately non-Boussinesq mixed convection. *Phys. Rev.* E **81** (2), 026301.

SUSLOV, S.A. & PAOLUCCI, S. 1999 Nonlinear stability of mixed convection flow under non-Boussinesq conditions. Part 1. Analysis and bifurcations. *J. Fluid Mech.* **398**, 61–85.

SUTHERLAND, W. 1893 The viscosity of gases and molecular force. *Lond. Edinb. Dublin Phil. Mag. J. Sci.* **36**, 507–531.

TALBOT, L., CHENG, R.K., SCHEFER, R.W. & WILLIS, D.R. 1980 Thermophoresis of particles in a heated boundary layer. *J. Fluid Mech.* **101**, 737–758.

TAN, T. & CHEN, Y. 2010 Review of study on solid particle solar receivers. *Renew. Sust. Energ. Rev.* **14**, 256–276.

TOM, J. & BRAGG, A.D. 2019 Multiscale preferential sweeping of particles settling in turbulence. *J. Fluid Mech.* **871**, 244–270.

VERZICCO, R. & ORLANDI, P. 1996 A finite-difference scheme for three-dimensional incompressible flows in cylindrical coordinates. *J. Comput. Phys.* **123** (2), 402–414.

WANG, B.-F., ZHOU, Q. & SUN, C. 2020 Vibration-induced boundary-layer destabilization achieves massive heat-transport enhancement. *Sci. Adv.* **6** (21), eaaz8239.

WANG, G. & RICHTER, D. 2020 Multiscale interaction of inertial particles with turbulent motions in open channel flow. *Phys. Rev. Fluids* **5**, 044307.

WANG, L.-P. & MAXEY, M.R. 1993 Settling velocity and concentration distribution of heavy particles in homogeneous isotropic turbulence. *J. Fluid Mech.* **256**, 27–68.

WANG, Q., XIA, S.-N., YAN, R., SUN, D.-J. & WAN, Z.-H. 2019 Non-Oberbeck–Boussinesq effects due to large temperature differences in a differentially heated square cavity filled with air. *Intl J. Heat Mass Transfer* **128**, 479–491.

WHITEHEAD, J.P. & DOERING, C.R. 2011 Ultimate state of two-dimensional Rayleigh–Bénard convection between free-slip fixed-temperature boundaries. *Phys. Rev. Lett.* **106**, 244501.

XIA, K.-Q. 2013 Current trends and future directions in turbulent thermal convection. *Theor. Appl. Mech. Lett.* **3**, 052001.

XIA, S.-N., WAN, Z.-H., LIU, S., WANG, Q. & SUN, D.-J. 2016 Flow reversals in Rayleigh–Bénard convection with non-Oberbeck–Boussinesq effects. *J. Fluid Mech.* **798**, 628–642.

XU, A., TAO, S., SHI, L. & XI, H.-D. 2020 Transport and deposition of dilute microparticles in turbulent thermal convection. *Phys. Fluids* **32**, 083301.

XU, W., WANG, Y., HE, X., WANG, X., SCHUMACHER, J., HUANG, S. & TONG, P. 2021 Mean velocity and temperature profiles in turbulent Rayleigh–Bénard convection at low Prandtl numbers. *J. Fluid Mech.* **918**, A1.

YANG, J.-L., ZHANG, Y.-Z., JIN, T.-C., DONG, Y., WANG, B.-F. & ZHOU, Q. 2021 The *Pr*-dependence of the critical roughness height in two-dimensional turbulent Rayleigh–Bénard convection. *J. Fluid Mech.* **911**, A52.

YANG, W., WANG, B.-F., TANG, S., ZHOU, Q. & DONG, Y. 2022*a* Transport modes of inertial particles and their effects on flow structures and heat transfer in Rayleigh–Bénard convection. *Phys. Fluids* **34**, 043309.

YANG, W., ZHANG, Y.-Z., WANG, B.-F., DONG, Y. & ZHOU, Q. 2022*b* Dynamic coupling between carrier and dispersed phases in Rayleigh–Bénard convection laden with inertial isothermal particles. *J. Fluid Mech.* **930**, A24.

ZAMANSKY, R., COLETTI, F., MASSOT, M. & MANI, A. 2014 Radiation induces turbulence in particle-laden fluids. *Phys. Fluids* **26** (7), 111–133.

ZAMANSKY, R., COLETTI, F., MASSOT, M. & MANI, A. 2016 Turbulent thermal convection driven by heated inertial particles. *J. Fluid Mech.* **809**, 390–437.

ZHANG, Y., ZHOU, Q. & SUN, C. 2017 Statistics of kinetic and thermal energy dissipation rates in two-dimensional turbulent Rayleigh–Bénard convection. *J. Fluid Mech.* **814**, 165–184.

ZONTA, F., MARCHIOLI, C. & SOLDATI, A. 2008 Direct numerical simulation of turbulent heat transfer modulation in micro-dispersed channel flow. *Acta Mechanica* **195** (1–4), 304–326.